The Active Optics system of the VLT Survey Telescope

PIETRO SCHIPANI,[1,*] LOTHAR NOETHE,[2] DEMETRIO MAGRIN,[3] KONRAD KUIJKEN,[4] CARMELO ARCIDIACONO,[5] JAVIER ARGOMEDO,[2] MASSIMO CAPACCIOLI,[1,6] MASSIMO DALL'ORA,[1] SERGIO D'ORSI,[1] JACOPO FARINATO,[3] DAVIDE FIERRO,[7] RONALD HOLZLÖHNER,[2] LAURENT MARTY,[1] CESARE MOLFESE,[1] FRANCESCO PERROTTA,[1] ROBERTO RAGAZZONI,[3] SALVATORE SAVARESE,[1,8] ANDREW RAKICH,[2] AND GABRIELE UMBRIACO[9]

[1]*Istituto Nazionale di Astrofisica – Osservatorio Astronomico di Capodimonte, Via Moiariello 16, I-80131 Naples, Italy*
[2]*European Southern Observatory, Karl-Schwarzschild-Str.2, D-85748 Garching bei München, Germany*
[3]*Istituto Nazionale di Astrofisica – Osservatorio Astronomico di Padova, Vicolo dell'Osservatorio 5, I-35122 Padua, Italy*
[4]*Leiden Observatory, Leiden University, P.O. Box 9513, NL-2300 RA Leiden, Netherlands*
[5]*Istituto Nazionale di Astrofisica – Osservatorio Astronomico di Bologna, Via Ranzani 1, I-40127 Bologna, Italy*
[6]*University of Naples Federico II, C.U. Monte S. Angelo,Via Cinthia, I-80126 Naples, Italy*
[7]*Istituto Nazionale di Astrofisica, Viale del Parco Mellini 84, I-00136 Rome, Italy*
[8]*University of Naples Federico II, DIETI, Via Claudio 21, I-80125 Naples, Italy*
[9]*University of Padua, Vicolo dell'Osservatorio 3, I-35122 Padua, Italy*
**Corresponding author: pietro.schipani@oacn.inaf.it*

Received XX Month XXXX; revised XX Month, XXXX; accepted XX Month XXXX; posted XX Month XXXX (Doc. ID XXXXX); published XX Month XXXX

This paper describes the active optics system of the VST (VLT Survey Telescope), the 2.6-m survey telescope designed for visible wavelengths of the European Southern Observatory at Cerro Paranal, in the Atacama desert. The telescope is characterized by a wide field of view (1.42 degree diameter), leading to tighter active optics than in conventional telescopes, in particular for the alignment requirements. We discuss the effects of typical error sources on the image quality and present the specific solutions adopted for wavefront sensing and correction of the aberrations, which are based on the shaping of a monolithic primary mirror and the positioning of the secondary in 5 degrees of freedom. © 2015 Optical Society of America

OCIS codes: *(220.1000) Aberration compensation; (220.1080) Active or adaptive optics; (220.1140) Alignment; (350.1260) Astronomical optics; (350.1270) Astronomy and astrophysics; (110.1080) Active or adaptive optics; (110.6770) Telescopes.*

http://dx.doi.org/10.1364/AO.99.099999

1. INTRODUCTION

The active optics [1-3] was invented at the European Southern Observatory (ESO) and first applied to the NTT telescope [4-8], enabling an historic improvement in the image quality of optical telescopes. Since then, it has been introduced in the design of most telescopes with mirror diameters of 2 metres or more. Nevertheless, the number of existing systems is still rather small, limited to the 2-m to 10-m telescopes built in the last two decades. Although the same basic concept is always adopted, the implementation is usually different.

After the NTT, other active optics systems based on thin meniscus primary mirrors have been the 8-m class ESO VLT [9-11], GEMINI [12] and SUBARU [13], the 4-m class TNG [14], SOAR [15], VISTA [16] and DCT [17]. Other active optics telescopes with monolithic primaries, but using lightweight honeycomb blanks, are the 3.5-m WIYN telescope [18], the 6.5-m MMT [19], the two 6.5-m Magellan telescopes [20], and the 2x8.4-m Large Binocular Telescope [21]. The two 10-m Keck [22] and the 10.4-m GTC [23] are also based on active optics but their primary mirror is segmented rather than monolithic.

Recently, the emerging class of wide-field telescopes (e.g. VST, VISTA and the future LSST [24]) is imposing tighter requirements for the alignment and, therefore, for the active optics systems.

In this paper, we describe the active optics system of the VST [25] (Fig. 1), the result of a joint venture between ESO and the Capodimonte Astronomical Observatory in Naples, formerly an independent institution and since 2002 a structure of the Italian National Institute for Astrophysics (INAF). It is a wide-field optical imaging telescope with a 2.6-metre aperture operating from the ultraviolet to the near-infrared (z'-band) with a corrected field of view of 1.42 degrees in diameter, allowing for an inscribed square field of a net 1 degree in size. Currently, it is the largest telescope in the world designed specifically for surveying the sky in visible light. Its focal plane instrument OmegaCAM [26] is a large camera contributed by the OmegaCAM consortium (Netherlands, Germany, Italy and ESO). It is composed of a mosaic of 32 2Kx4K scientific CCDs arranged in a 8x4 matrix, with a pixel size of 15μm and a scale of 0.21"/pixel. In 2011, the

commissioning phase ended and the VST started its regular operations [27].

The paper is organized as follows. Section 2 describes the optical system with particular reference to the most relevant aspects within the active optics framework. Section 3 shows the aberration modes corrected by the telescope, discussing their dependence on the physical system. Section 4 discusses the effect of the most typical error sources on the images, whose patterns can be more easily recognized in a wide-field telescope. Section 5 shows the system architecture and the overall logic of the corrections. Section 6 summarizes the primary mirror support system design and its implementation. Section 7 describes the secondary mirror correction system. Section 8 summarizes the wavefront sensing design and implementation aspects. Section 9 outlines the status of the system and its future perspectives.

2. OPTICAL SYSTEM AND FIELD ABERRATIONS

The VST is an F/5.5 two mirror telescope with a lens corrector designed to flatten the field dependent aberrations, improving the image quality on a wide field of view. The primary mirror is a concave 2.6-m hyperbolic meniscus with a 60 cm central hole and 140 mm thickness, the 0.9-m secondary mirror is convex and hyperbolic. Both mirrors were made of Astro-Sitall by the Russian LZOS company.

The optical configuration is different from a Cassegrain telescope, which is corrected for spherical aberration, or a Ritchey-Chretien telescope, where also the field coma is corrected. In the VST the dependencies of the dominant field aberrations curvature, third-order coma and third-order astigmatism on the radial field coordinate σ and the angular field coordinate φ are more complicated.

The aperture dependencies of the dominant field aberrations are expressed in terms of Zernike polynomials, using the Zemax ordering as shown in Table 1.

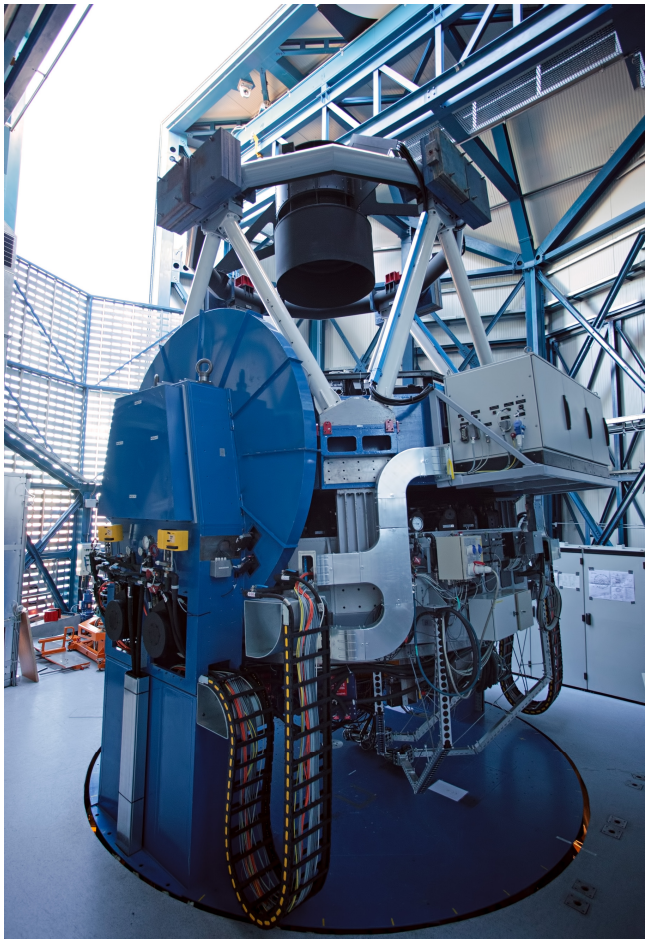

Fig. 1: The VLT Survey Telescope (Credit: ESO)

Table 1: Zernike Standard Polynomials (Zemax™ definition), first eight modes.

Z1	1
Z2	$2\rho\cos(\varphi)$
Z3	$2\rho\sin(\varphi)$
Z4	$\sqrt{3}(2\rho^2-1)$
Z5	$\sqrt{6}\rho^2\sin(2\varphi)$
Z6	$\sqrt{6}\rho^2\cos(2\varphi)$
Z7	$\sqrt{8}(3\rho^3-2\rho)\sin(\varphi)$
Z8	$\sqrt{8}(3\rho^3-2\rho)\cos(\varphi)$

Their field dependencies strongly deviate from the classical linear (for coma) and quadratic (for defocus and astigmatism) dependencies, originating from 3rd order aberration. Instead, they are well described adding higher order terms in the radial field coordinate:

$$Z_4(\sigma) = c_{40} + c_{42}\sigma^2 + c_{44}\sigma^4 \quad (1)$$

$$Z_6(\sigma) = c_{62}\sigma^2 + c_{64}\sigma^4 \quad (2)$$

$$Z_8(\sigma) = c_{81}\sigma + c_{83}\sigma^3 + c_{85}\sigma^5 \quad (3)$$

The coefficients c_{ij} (Table 2) strongly depend on the wavelength. The Fig. 2, Fig. 3 and Fig. 4 show the field dependencies of the dominant field aberrations on the field radius at the central wavelengths of the camera filters.

The properties of field aberrations in the VST are particularly relevant for several reasons discussed hereafter.

The first reason is that the VST Shack-Hartmann (section 8) measures the sum of these aberrations and the ones introduced by the deviations of the optical system from the ideal case. The former are present by design and the latter shall be corrected, hence the nominal field-dependent aberrations have to be subtracted from the measured ones.

Also, the theoretical field astigmatism data were used for the alignment during the telescope commissioning phase [28]. The first step was the removal of coma in the field center. This was obviously not sufficient, because the zero-coma condition only guarantees the axes of primary and secondary mirrors intersect at the so-called neutral (or "coma-free") point. There is still an infinite number of zero-coma configurations associated to the rotation of the secondary mirror around a pivot corresponding to the neutral point, with only one corresponding to the perfect alignment of the mirrors. All the others are misaligned configurations, where the optical system is affected by an amount of linear astigmatism (i.e. increasing linearly with the field) proportional to the rotation around the pivot point. Therefore, the second step of the alignment procedure was the measurement of misalignment starting from the zero-coma condition, which was performed evaluating the astigmatism at several off-axis field points and comparing the measurements with the theoretical values. The additional linear astigmatism was then removed by counter-rotating the secondary mirror around the neutral point. The wide-field of the VST greatly helps to get a good signal to noise ratio during these measurements.

Finally, the field-dependent aberrations analysis gives many insights into the ellipticities pattern of stars in the VST frames. Ellipticities are generated by single aberrations like coma or by pairs of aberrations, with the pair of defocus and third-order astigmatism usually being the dominant one [29].

Table 2: Coefficients of dominant field aberrations at the central wavelengths of the camera filters.

λ [μm]	c_{40}	c_{42}	c_{44}	c_{81}	c_{83}	c_{85}	c_{62}	c_{64}
0.354	169.3	2050.5	−5437.0	447.3	−657.0	236.5	341.5	−1183.7
0.412	−139.9	3006.7	−5370.3	691.0	−661.0	230.4	469.6	−1171.6
0.439	−238.7	3325.7	−5348.1	772.2	−662.3	228.4	512.2	−1167.6
0.475	−342.7	3669.4	−5324.1	859.7	−663.6	226.3	558.2	−1163.2
0.551	−495.6	4190.6	−5287.8	992.3	−665.6	223.1	627.8	−1156.6
0.625	−593.7	4535.8	−5263.8	1080.2	−666.8	221.0	673.9	−1152.2
0.756	−707.1	4946.5	−5235.2	1184.6	−668.2	218.5	728.7	−1147.0
0.880	−780.5	5219.4	−5216.3	1254.0	−669.1	216.8	765.1	−1143.5

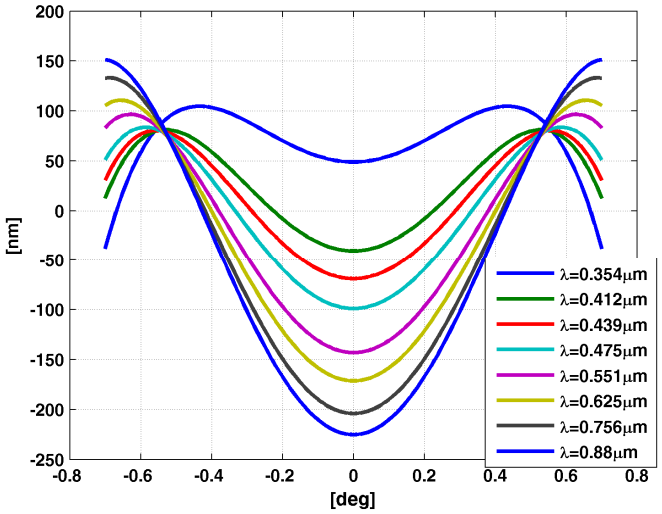

Fig. 2: Defocus as a function of radial field coordinate σ and wavelength λ.

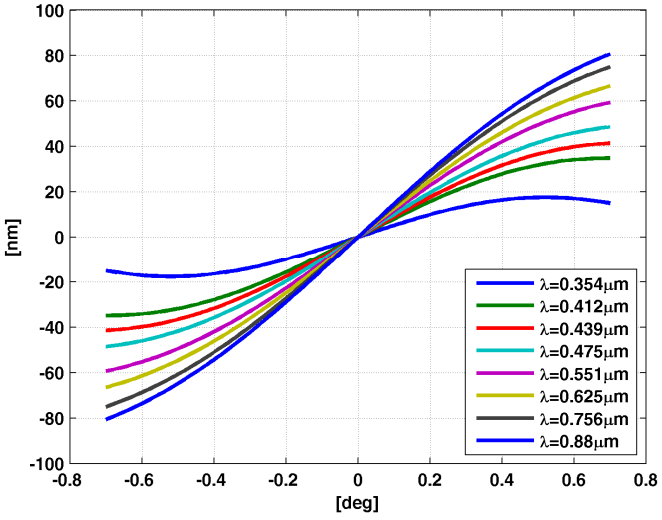

Fig. 3: Coma as a function of radial field coordinate σ and wavelength λ.

As any other telescope affected by field aberrations, the VST has a rotationally symmetrical pattern of ellipticities in the field even in the ideal condition of perfect alignment and mirror shapes (Fig. 5). The VST pattern is dominated by the effect of the pair of defocus and astigmatism. As the field is curved, the ideal condition is a compromise where the best focus (c_{def} =0) is not in the center as usual, but approximately half-way to the edge of the field: the ring of zero ellipticity visible in Fig. 5 corresponds to the zero defocus condition. Furthermore, the ellipticities in the center, inside the zero-defocus circle, are perpendicular to the ellipticities outside the circle. The reason is the well-known property of the ellipticity of an astigmatic image, which rotates by 90 degrees from intra- to extra-focal position.

For a real image, the moduli of the measured root mean squares σ_l of the long axis and σ_s of the short axis depend on the seeing conditions. Also, the measured angles α are ambiguous, as α and α+π are equivalent. An alternative definition of the ellipticity is given, unambiguous and seeing independent, in order to compare the optical theory with the measured parameters [29]. One can assume that σ_l^2 and σ_s^2 are the quadratic sums of contributions from the seeing on the one hand and coma and the products of pairs of aberrations on the other hand. If the difference:

$$\varepsilon = \sigma_l^2 - \sigma_s^2 \qquad (4)$$

is defined as the ellipticity modulus, the dependence on the seeing vanishes. The ambiguity on the angle is solved by defining the angle of the ellipticity as 2α rather than α. However, the spot size, defined as $(\sigma_l^2-\sigma_s^2)/2$, is at best equal to the contribution from the seeing. Fig. 6 represents the pattern of the ellipticity vector $\vec{\varepsilon}$ with doubled angles 2α, corresponding to Fig. 5.

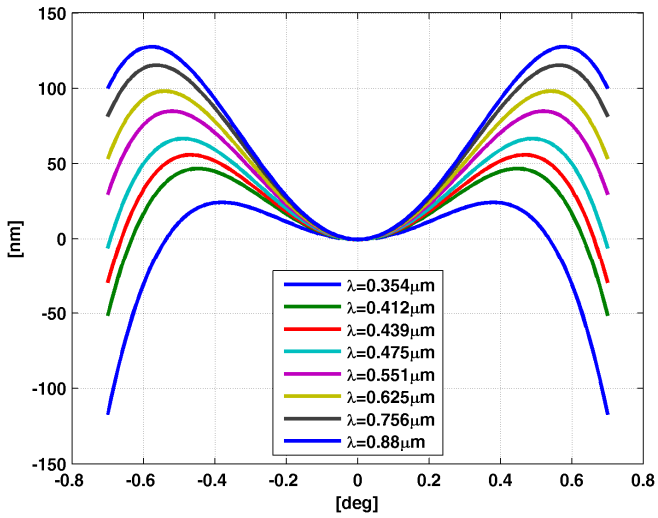

Fig. 4: Astigmatism as a function of radial field coordinate σ and wavelength λ.

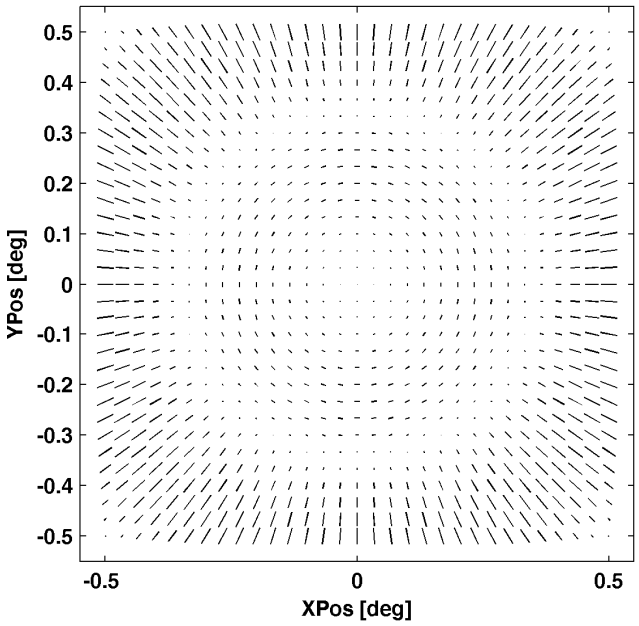

Fig. 5: Ideal pattern of measured ellipticities for VST with true angles α. The modulus depends on wavelength and seeing conditions.

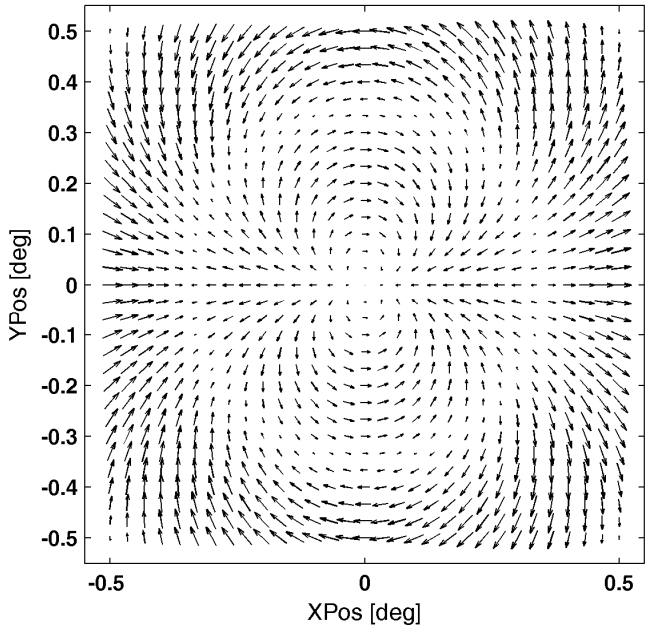

Fig. 6: Ideal pattern of ellipticities for VST with doubled angles 2α and modulus defined as in Eq. (4), depending only on the wavelength.

3. ABERRATION MODES

The VST wavefront sensors and the correction devices are designed to measure and correct the modes listed in Table 3.

Type 1 modes are Zernike polynomials, type 2 modes are the elastic modes of the primary mirror. Both sets are composed of mutually orthogonal functions; their mix causes a small but negligible non-orthogonality.

On the one hand, the Zernike polynomials describe defocus and coma, optically corrected by movements of the secondary mirror. On the other hand, the aberrations corrected by changing the shape of the primary are better described by the primary mirror natural vibration modes. They form an orthonormal basis with analytic expressions depending on the mirror material and geometry, with shapes similar to the Zernike modes. The determination of the analytic expressions of the elastic modes involves the solution of the equations describing the minimum energy modes of a thin shallow shell, imposing the free edge boundary conditions. The results of the computation are the radial parts of the mirror elastic modes $u_{n,m}(r)$, depending on the symmetry *n* and the order *m*.

One of the advantages of elastic modes is that the maximum correction forces are lower than the ones for the Zernike modes, thus allowing a wider correction range. As an example, consider the elastic mode $e_{2,1}$ and the corresponding Zernike polynomial Z_5, whose radial dependence is shown in Fig. 7. For the same surface r.m.s., the maximum forces in the set of forces needed for the correction of the elastic mode are about 6 times smaller than for the Zernike mode.

For the comprehensive theory and justification for the use of minimum energy modes see [30].

Table 3: Aberration modes corrected in VST. T=Type; S=Symmetry; O=Order. Type 1: Zernike; type 2: Elastic Mode. Sph3=3rd order spherical; Ast3=3rd order astigmatism

T	S	O	Description	Expression
1	0	2	$Z_{0,2}$	$r^2-\frac{1}{2}$
2	0	2	$e_{0,2}$ (~Sph3)	
1	1	2	$Z_{1,2}$	$\left(r^3-\frac{2}{3}r\right)\cos\theta$
2	2	1	$e_{2,1}$ (~Ast3)	
2	3	1	$e_{3,1}$ (~Trefoil)	
2	4	1	$e_{4,1}$ (~Tetrafoil)	

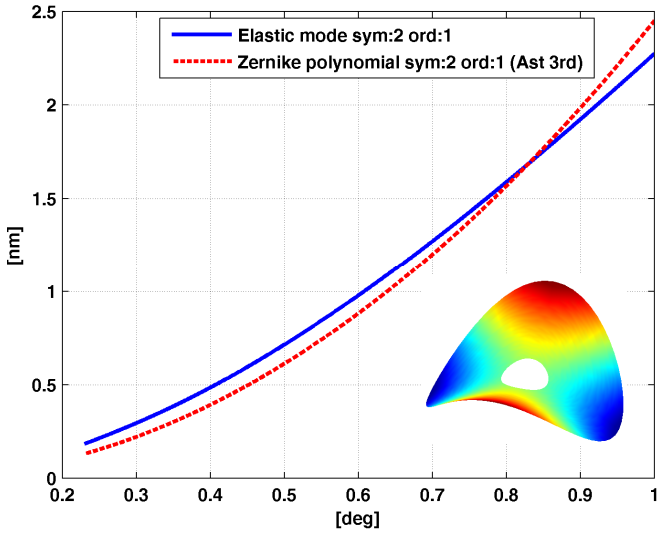

Fig. 7: Primary mirror elastic mode $e_{2,1}$ compared with its Zernike equivalent (radial function).

4. EFFECTS OF ERROR SOURCES

Any individual error source has a different effect on the pattern of ellipticities and spot sizes of the VST wide-field image, modifying the ideal pattern of Fig. 5, i.e. most of the telescope defects leave a unique signature. In case one defect dominates over all the others, it can be identified even from visual inspection of the ellipticity pattern, without a wavefront sensor. However, during normal operations all error sources are mixed together with small individual contributions, creating patterns often without a dominant signature. Complex algorithms to disentangle the error contributions are under development within the VST framework and look promising for future wavefront sensing implementations [29, 31].

A special attention has to be paid to telescope error sources that can produce similar effects on the ellipticity pattern. An example are guiding errors (caused by the telescope mount and control system),

constant coma across the whole field (caused by misalignment) or the combination of defocus and third-order astigmatism, both of them constant across the field. Without the presence of other aberrations, each of these three error sources will generate constant ellipticities with identical angles and modules across the whole field.

A. Despace of mirrors

Despace of mirrors along the optical axis causes a defocus that is added to the nominal field curvature, modifying the pattern of Fig. 5. The circle of zero defocus and ellipticity shrinks (Fig. 8), enlarges or even disappears when the additional defocus overcomes limit values which depend on the wavelength. All patterns are still rotationally symmetric as expected.

B. Primary mirror warping

Usually, constant astigmatism is the strongest aberration caused by a warping of the primary mirror. It is constant in modulus and angle across the field and introduces an asymmetry in the system, thus the resulting pattern of ellipticities is not rotationally symmetric. Without additional defocus the circle, where the ellipticities vanish, remains the same (Fig. 9). The angles of the ellipticities rotate with the true angles of the astigmatism.

C. Rotation of secondary mirror around neutral point

As discussed in section 2, after a coma correction the telescope is in general still not aligned, with the secondary mirror rotated around the neutral point causing linear astigmatism. The modulus of linear astigmatism increases linearly with the distance from the center of the field; its angle depends on the direction of the misalignment. The ellipticities rotate with half the field angle (Fig. 10). For a detailed theory of linear astigmatism and its relations with primary mirror astigmatism see [32-36].

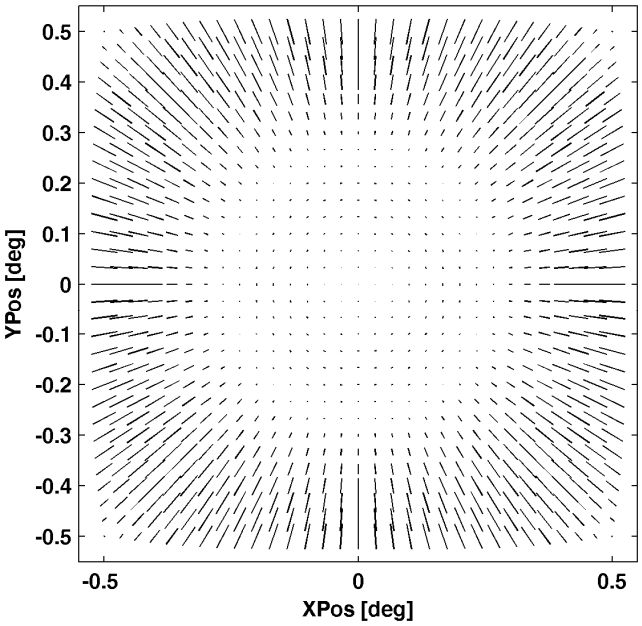

Fig. 8: Positive constant defocus shrinking the zero defocus circle (ellipticities with true angle α).

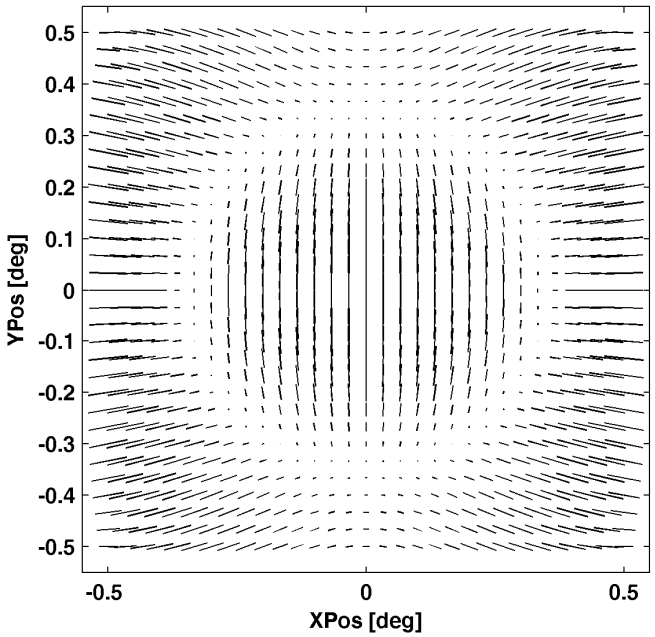

Fig. 9: Effect of adding constant astigmatism (ellipticities with true angle α).

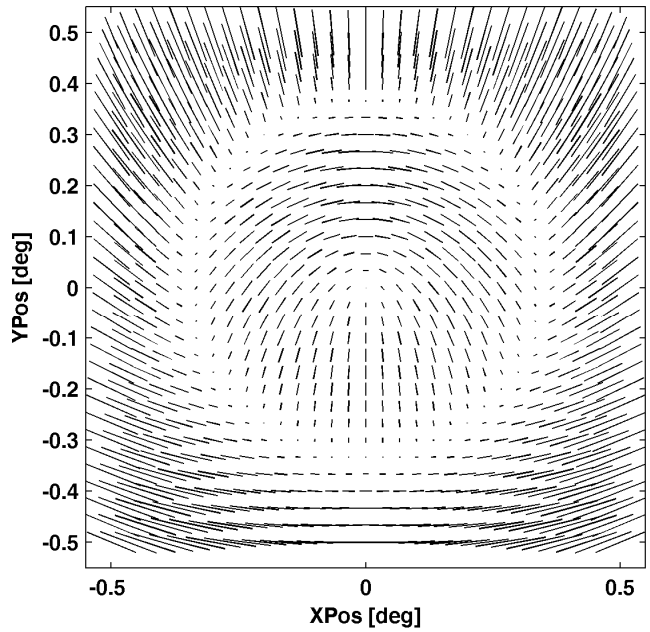

Fig. 10: Effect of adding linear astigmatism due to a rotation of the secondary mirror around the coma-free point Y-axis (ellipticities with true angle α).

D. Focal plane tilt

The focal plane can be wrongly tilted because of two reasons:

- incorrect planarity of the camera on the rotator flange
- incorrect alignment of the rotator axis with the optical axis

In both cases the defocus pattern is modified, deviating from its original symmetry. An amount of defocus increasing linearly along a certain direction with the field radius is added to the nominal field curvature creating an asymmetry in the defocus and, therefore, also in the ellipticity patterns across the field.

The two causes of tilt can be disentangled by the analysis of two images taken before and after a 180 degree rotation of the instrument. In the first case, the tilt of defocus across the detector remains the same, whereas, in the second case, it changes by 180 degrees.

In all cases, the modification of the defocus pattern causes a non rotationally symmetric distribution of the ellipticities, as shown in Fig. 11 for a tilt around the X-axis.

The focal plane tilt cannot be actively controlled. During the commissioning phase, it has been compensated with mechanical interventions [28].

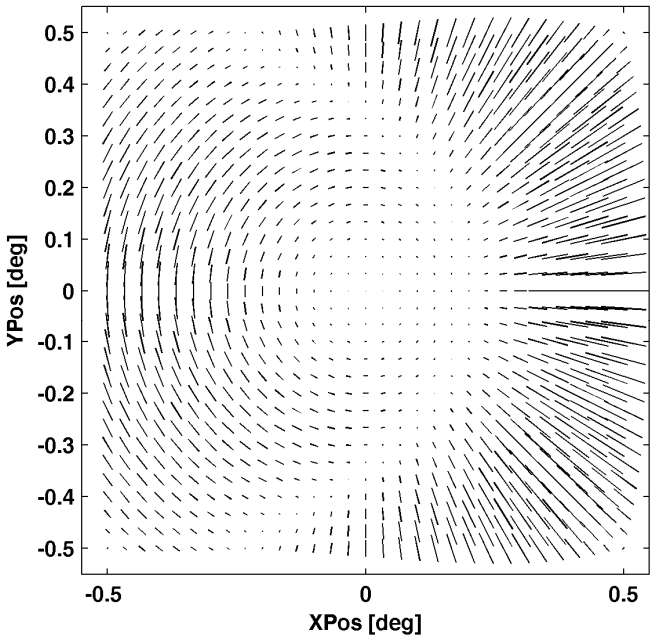

Fig. 11: Effect of a tilt of the focal plane for a tilt around the X-axis (ellipticities with true angle α).

5. SYSTEM ARCHITECTURE

The VST active optics system is based on wavefront sensing and correcting devices, which are actuators for modifying the shape of the primary mirror and for the positioning of the secondary mirror. There are two wavefront sensors, one in the telescope and another in the camera. The one in the telescope is a Shack-Hartmann sensor installed on a probe system, which can be positioned anywhere in the field, using a (ρ,θ) motorized probe. Nevertheless, as the probe causes vignetting and its physical movement adds an overhead to operations, the sensor usually used is the one in the camera. It is based on the curvature principle and has neither moving parts nor vignetting problems. Nonetheless, the Shack-Hartmann sensor has been extremely useful during the telescope commissioning when the camera was not yet available, and its results have been used to calibrate the curvature sensor.

The actuation system is composed of a hexapod, which moves the secondary mirror, and four rings of force actuators supporting the primary mirror, which is also protected by a safety system [37] from possible damages caused by earthquakes. The commands to the actuators can come from an online computation of corrections coming from the wavefront sensor, or from the interpolation of look-up tables containing calibrated values depending on zenith angle and temperature.

6. PRIMARY MIRROR SUPPORT AND CORRECTION SYSTEM

The axial system supports the component of the weight of the mirror along the optical axis, depending on the zenith angle. It corrects the aberrations by tuning the optical surface with a pattern of active forces whose resultant is ideally zero. The non zero resultant, caused by small inaccuracies in actuator settings, is taken by the hard points.

The support geometry is the result of an optimization problem. The minimization of the r.m.s deformation σ_w of the mirror surface, when the mirror rests on concentric rings at zenith, was chosen as the criterion. Compared with the alternative minimization of the r.m.s. of the slope error, it allowed for a more uniform load density on the rings. Two options with three and four rings were considered. The one with four rings required smaller correction forces and gave more freedom for the aberration corrections, although the implementation of the four ring solution was more expensive and complex. The optimization was done considering the two options of mirror full aperture and clear aperture. The minimum r.m.s. was almost identical. However, the ring radii obtained with the optimization across the full aperture was chosen, since the rings were more evenly spaced.

Fig. 12 shows the result of the optimization problem for a four rings continuous support over the full aperture. The X-Axis is the normalized radius from the inner to the outer radius, the Y-axis represents the wavefront error generated by the deformation of the mirror surface. The vertical bars represent the radial positions of the rings.

The radii and the fractions of the weight supported by the four rings are listed in Table 4.

Table 4: Axial support geometry

Ring	Norm. Radius	Weight Fraction
1	0.3217	0.134410
2	0.5298	0.228627
3	0.7310	0.304733
4	0.9246	0.332230

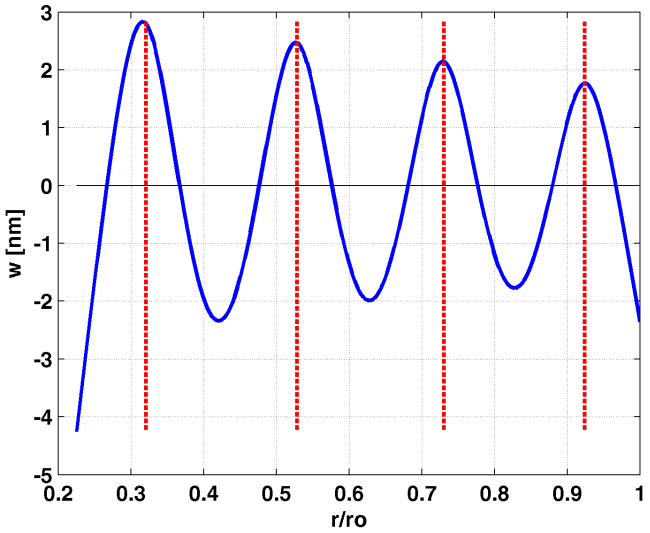

Fig. 12: Wavefront error caused by the deformation of the mirror surface on a four continuous rings support. The dashed vertical bars represent the rings radii.

The number of supports for each ring was chosen such that the azimuthal distances between the supports are similar to the radial ones. These numbers are always multiples of 3, so the whole system has a threefold symmetry. There are 84 supports (81 actuators and 3 hard points) in all, distributed on 4 rings with 12, 18, 24, 30 supports (Fig. 13).

Three hard points are placed on the third ring at 120°, defining the plane of the mirror. The mirror plane can be adjusted for alignment purposes by acting on their heights, which are controlled by a motorized system. The stiffness of the hard points is one order of magnitude greater than the stiffness of the actuators.

The force delivered by the supports is transmitted to the mirror by means of push-only connections. For mirror safety reasons, the maximum force is limited by electro-mechanical protections and by software. More details on actuators and the electro-mechanics design are given in [38].

The calibration forces for the correction of the aberration modes have been computed solving an optimization problem, where the objective parameter to minimize was the difference between the r.m.s. values of the desired deformation and the one generated by the support forces. For rotational symmetries n>1, this method led to a system of 4 linear equations in 4 unknowns (the calibration forces at the 4 radii). For rotational symmetries n=0 and n=1 the condition of equilibrium of forces and equilibrium of moments, respectively, were also imposed using the Lagrange multiplier method, leading to a system of 5 linear equations in 5 unknowns.

The results are summarized in Table 5, which shows the forces for the correction of 10 nm of the aberration modes corrected during normal operations.

Table 5: Calibration forces [N] corresponding to 10 nm aberration coefficients

Elastic Mode (sym, ord)	Ring1	Ring2	Ring3	Ring4
$e_{0,2}$	6.77	–3.94	–4.36	3.14
$e_{2,1}$	0.02	0.05	0.08	0.11
$e_{3,1}$	0.05	0.21	0.44	0.67
$e_{4,1}$	0.05	0.48	1.22	2.18

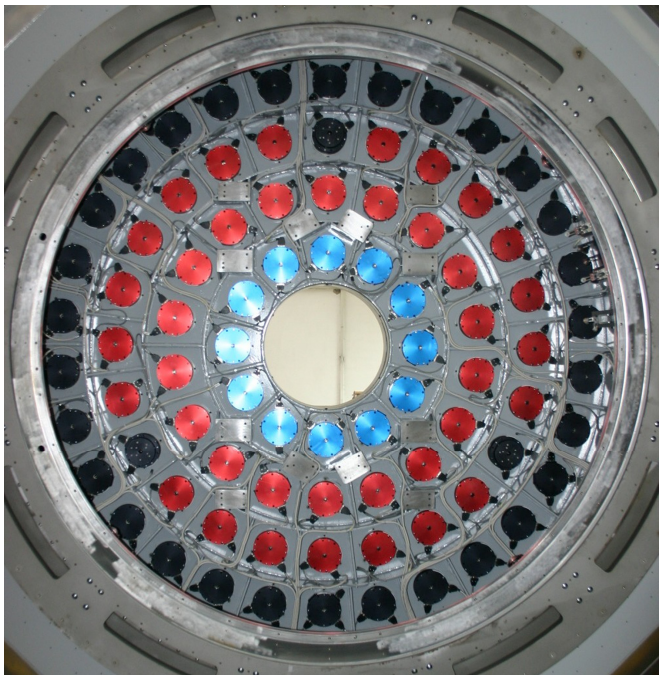

Fig. 13: Primary mirror axial supports (backside).

Notably, the $e_{0,2}$ mode needs the largest forces, thus the wavefront correction budget is smaller for this mode. However, the bulk of aberrations generated by the primary mirror is astigmatism or $e_{2,1}$ in terms of elastic modes; Table 5 shows that $e_{2,1}$ can be corrected with much smaller forces than any other mode.

Further details for the analytical expressions for the elastic modes and the computation of the calibration forces in the VST case are discussed in [39].

The lateral system supports the component of the weight of the mirror perpendicular to the optical and altitude axes. It is based on 24 astatic lever supports and three lateral fixed points defining the position of the mirror in its plane. The lateral forces are distributed according to the Schwesinger [40] theory. For practical reasons the forces are applied at the center of the outer rim, which is not in the plane containing the center of gravity of the curved mirror. Therefore, the lateral forces must also have Z-components (i.e. orthogonal to the mirror plane), which balance the moment created because the mirror is not laterally supported under its center of gravity.

Fig. 14 shows the radial functions of the wavefront aberrations generated by the lateral support for various values of the force ratio β between the weight that is tangentially supported and the total weight. The system has been designed with β=0.75, i.e. 75% of the lateral weight is supported tangentially and 25% radially. The directions of forces in the XY-plane are shown in Fig. 15.

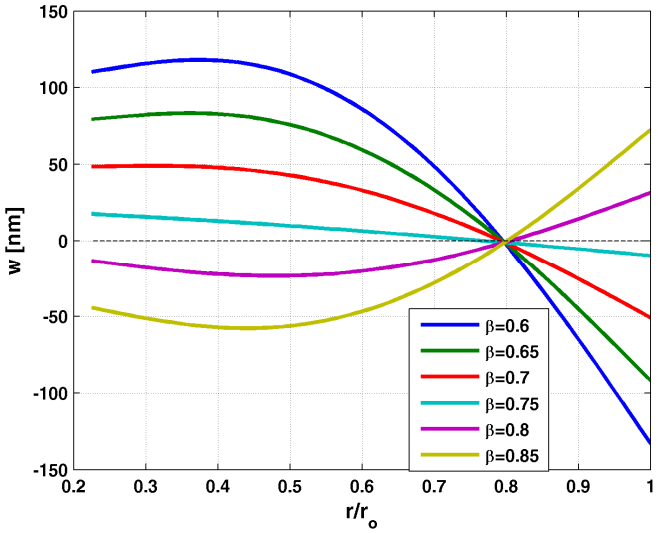

Fig. 14: Radial wavefront aberrations for different ratios β values of the total lateral weight supported by tangential forces.

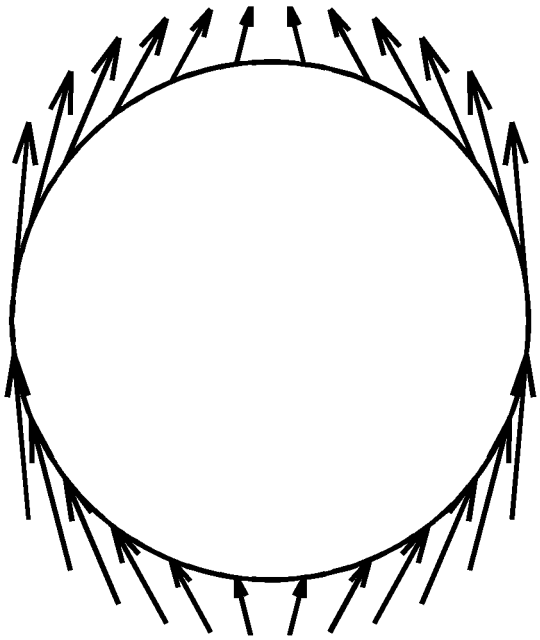

Fig. 15: Components of the lateral forces in the XY-plane for β=0.75.

A. Operational aspects

When the telescope tube is inclined towards the horizon, the passive axial forces are not adjusted automatically as in the lateral support system using astatic levers.

Thus, the rotation of altitude would continuously create an incorrect load on the three axial hard points, causing an increasing amount of trefoil aberration, combined with a small defocus. The defocus is generated by a deformation of the mirror as well as by an axial shift due to the finite, although high, stiffness of the hard points. During tracking, this potential effect is counter-balanced by the control system through the implementation of a background task which periodically regulates the load on the three hard points. Actually, as the hard points

are not force-controlled, this operation is done indirectly, slightly loading or unloading the 81 active supports through a differential correction. Although this correction is activated only during tracking, the telescope can safely rotate without the activation of this background task in any other case, e.g. for maintenance.

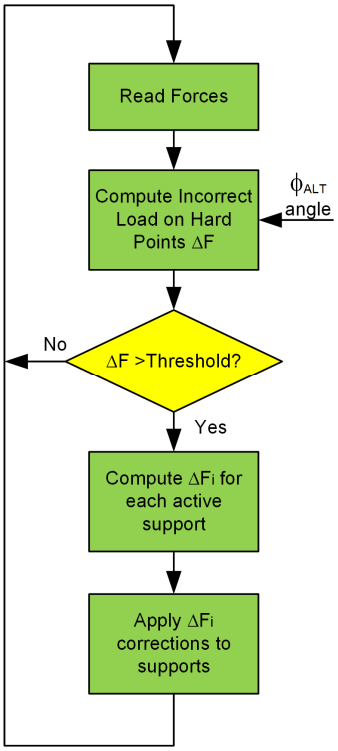

Fig. 16: Algorithm for passive force adjustments.

The background task loops continuously, with a configurable period. Nevertheless, the correction is physically performed only if the load error on the hard points is greater than a threshold F_{th}=3Kg.

This threshold comes from a tradeoff: it shall be small enough in order to allow the introduction of only negligible errors, but not too small to avoid false corrections due to inaccuracies in the measurement of loads of the axial fixed points. These measurements are less precise since the load cells on the fixed point must be able to measure 10 times larger forces than the load cells on the other 81 supports.

Roughly, the threshold value F_{th}=3Kg corresponds to an average error of 1Kg on each of the 3 hard points, which causes a defocus with a coefficient c_{def}=37nm and a negligible trefoil, both within the measurement noise.

When the zenith angle is large, the correction is triggered more frequently. This depends on the rate of change of the axial weight, which is a function of sin(ϕ_{ALT}). For a delta variation of altitude angle, the variation of the axial weight is:

$$\Delta W = W\left[\sin\left(\varphi_{ALT}\right) - \sin\left(\varphi_{ALT} - \delta\right)\right] \quad (5)$$

The background task runs every 10 seconds. With this frequency and at the maximum altitude velocity of v=13"/s, the maximum altitude variation is δ_{10}=0.036°. The maximum variation of the axial weight in 10 seconds would occur at the lowest limit of the altitude range, i.e. at ALT=20°. Under the most unfavorable conditions, the maximum variation of axial weight would then be ΔW_{max}=1.1Kg, well below F_{th}. Thus, in all conditions the background loop corrects the error immediately after it reaches the threshold, and the maximum error in terms of trefoil and defocus is always negligible.

The background correction forces are uniformly shared between the supports, i.e. all the supports on the same ring receive an identical differential correction, with a fraction according to the nominal distribution of forces on the four rings (Table 4). Thus, in practice no aberrations other than trefoil and defocus are altered by these small adjustments.

A semaphore provided by the VxWorks operating system prevents the overlap between the background task adjustments and the normal active optics corrections.

Further details on the primary mirror control software are given in [41].

7. SECONDARY MIRROR CORRECTION SYSTEM

The secondary mirror is actively controlled in order to correct defocus, coma and linear astigmatism. The relevant parameters for the VST and the correction device are discussed hereafter.

A. Corrections

1. Defocus

The despace of mirrors causes a proportional amount of defocus. The relation between the coefficient of r^2 defocus c_{def} measured by the wavefront sensor and the axial displacement Δz is:

$$\Delta z = \eta_{def} c_{def} \quad (6)$$

where η_{def}=-27.2 (dimensionless) is computed with ray-tracing.

2. Coma

The coma might be compensated through a simple tilt of the secondary mirror around the pole, or a decenter. However, both kind of motions would change the pointing of the telescope. On the contrary, a rotation around the centre of curvature of the mirror allows for a coma correction that does not move the image and is suitable for active corrections in closed loop. The decenter δ and rotation α are proportional according to Eq. (7), where $f_2^{'}$ is the focal length of the secondary mirror:

$$\alpha = -\frac{\delta}{2 f_2^{'}} \quad (7)$$

Consequently, the coma correction is described by a single parameter η_{coma}=-247.4 (dimensionless).

$$c_{coma} = \frac{\delta}{\eta_{coma}} \quad (8)$$

3. Linear astigmatism

The correction of linear astigmatism assumes that coma has already been removed, i.e. it starts from a zero coma condition. It is implemented by a rotation of the secondary mirror around the neutral point, which is by definition the pivot point along the optical axis around which the mirror can rotate without introducing coma. The neutral point position z_{cfp}=1073.8 mm is calculated by imposing that the coma contributions from a lateral decenter δ and a rotation $\alpha = -\delta / z_{cfp}$ cancel each other out.

B. Correcting device

The secondary mirror is assumed stiff, thus only its rigid body motions are controlled. It is supported by a passive astatic lever system based on the designs of the NTT and the TNG, both of them using counterweights. It supports the weight of the mirror, self-adjusting the force components acting on the mirror when the altitude angle changes. The mirror is positioned by a hexapod device (Fig. 17), i.e. a parallel robot also known as 6-6 Stewart platform. A fixed platform attached to the telescope is connected to a moving platform, which supports the mirror through six linear actuators with sub–µm

accuracy. The mechanics of the VST device is a replica of the TNG implementation, while the control system is totally different and improved. The solutions for inverse and forward kinematics are described in detail in [42]. Further details on the hexapod and its performance are discussed in [43].

Fig. 17: The VST hexapod.

8. WAVEFRONT SENSING

A. OmegaCAM sensor

During operation, the measurement of the wavefront aberrations can continuously be done by using the OmegaCAM curvature-sensing [44-45] system.

It consists of two CCDs at the edge of the field, taking exposures of a few seconds. By mounting one of them intra-focal and the other one extra-focal, they generate defocused star images, resembling donuts. The aberration coefficients are estimated by a fit of combinations of suitable basis function both to the edge shapes of the images as well as to the intensities inside the images. These basis functions correspond to a set of telescope aberrations that generate distinguishable changes in the pairs of images (Fig. 18).

Although the system has been working reliably since the start of telescope operations, the donuts algorithm [46] has been further developed to take into account seeing effects and to enable an additional closed loop correction of linear astigmatism.

B. Shack-Hartmann

As explained in Section 5, during normal operations the wavefront sensing is done by the camera, but for several reasons a Shack-Hartmann sensor is also available. According to the principle of Shack-Hartmann, a matrix of star spots is formed on a technical CCD (Fig. 19) and compared by software with a reference matrix recorded using an artificial reference light. Afterwards, the differences are used by the telescope control software to compute the coefficients of the aberration modes. As the displacements of the spots from the reference positions are proportional to the wavefront slopes, two alternatives have been considered to reconstruct the wavefront: the direct fit of the wavefront slopes to aberration coefficients, or the integration of the slopes to reconstruct the wavefront, followed by the fit of the aberration functions to the wavefront. We chose the first option to fit directly the derivatives of the modes to the slopes, because the limited number of spots in our system, due also to a considerable obscuration, would have caused inaccuracies in the integration of the slopes along rows and columns with just few spots.

During commissioning, we discovered that the wavefront sensor system itself was affected by a non-negligible amount of static aberrations. Therefore, although the active optics loop converged to small aberration coefficients after a few iterations, the telescope optics was still not in a well corrected state. An attractively easy method was implemented to measure and remove these static aberrations just by software, with no hardware intervention [47]. Indeed, it would be worth implementing a similar analysis in any similar active optics system, as the static aberrations are never rigorously zero.

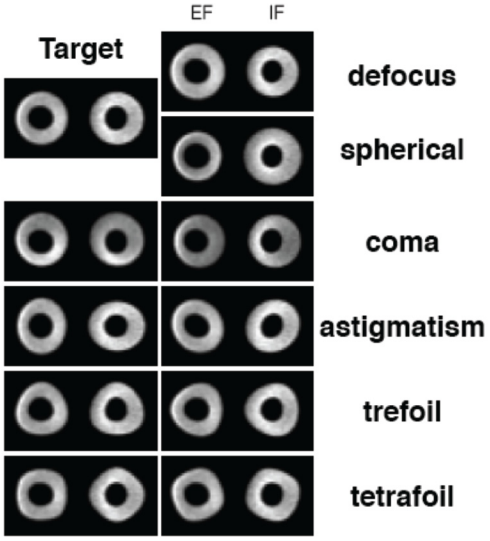

Fig. 18: Basis functions for donuts analysis.

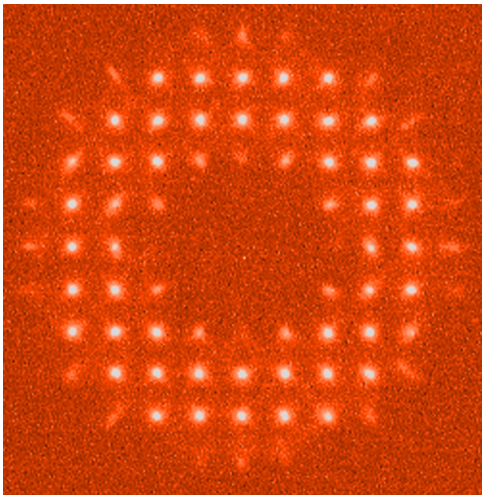

Fig. 19: One of the first VST Shack-Hartmann frames, taken at the beginning of the commissioning phase.

9. STATUS AND OUTLOOK

The active optics system of VST has been working reliably since the start of the commissioning at the beginning of 2011, in particular the primary mirror system, deemed the most critical item during the construction phase because of its poor accessibility and its delicate

task. The secondary mirror support was affected by a few sporadic failures, which were fixed by the ESO Paranal engineering staff. The wavefront sensing will be further upgraded, on the one hand by upgrading the donuts algorithm and on the other hand by introducing new techniques for wavefront measurements in wide field telescopes, based on the direct use of scientific images.

References

1. Wilson, R.N., "The history and development of the ESO active optics system", The Messenger 113, 2-9 (2003).
2. Noethe, L., "Active optics in modern, large optical telescopes", Progress in Optics 43, 3-69 (2002).
3. Noethe, L., and Wilson, R., "Active Thin-Mirror Telescopes", in Planets, Stars and Stellar Systems, Volume 1: Telescope and Instrumentation, Eds. T. Oswalt and I.S.McLean, Springer Verlag (2013), pp. 185-239.
4. Wilson, R.N., Franza, F., Noethe, L., "Active optics I: a system for optimizing the optical quality and reducing the costs of large telescopes", J. Mod. Opt. 34 (4), 485-509 (1987).
5. Noethe, L., Franza, F., Giordano, P., Wilson, R.N., Citterio, O., Conti, G., Mattaini, E., "Active optics II: Results of an experiment with a thin 1-m test mirror", J. Mod. Opt. 35 (9), 1427-1457 (1988).
6. Wilson, R.N., Franza, F., Giordano, P, Noethe, L., Tarenghi, M., "Active optics III: final results with the 1m test mirror and NTT 3.56m primary in the workshop", J. Mod. Opt. 36 (11), 1415-1425 (1989).
7. Wilson, R.N., Franza, F., Noethe, L., Andreoni, G., "Active optics IV: set-up and performance of the optics of the ESO New Technology Telescope (NTT) in the observatory", J. Mod. Opt. 38 (2), 219-243 (1991).
8. Noethe, L., Andreoni, G., Franza, F., Giordano, P, Merkle, F., Wilson, R.N., "Latest development of active optics of the ESO NTT and implications for the ESO VLT", Proc. SPIE 1542, 293-296 (1991).
9. Guisard, S., Noethe, L., Spyromilio, J., "Performance of active optics at the VLT", Proc. SPIE 4003, 154-164 (2000).
10. Guisard, S., Noethe, L., Spyromilio, J., Delgado, F., "Performance and improvements of active optics at the Very Large Telescope", Proc. SPIE 4837, 637-648 (2003).
11. Stanghellini, S., Legrand, P., Baty, A., Hovsepian, T., "Design and construction of the VLT primary mirror cell", Proc. SPIE 2871, 314-325 (1998).
12. Stepp, L., Huang, E., Cho, M., "Gemini primary mirror support system", Proc. SPIE 2199, 223-238 (1994).
13. Iye, M., Kodaira, K., "Primary mirror support system for the SUBARU telescope", Proc. SPIE 2199, 762-772 (1994).
14. Bortoletto, F., Fantinel, D., Ragazzoni, R. Bonoli, C., D'Alessandro, M., "Active optics handling inside Galileo telescope", Proc. SPIE 2199, 212-222 (1994).
15. Krabbendam, V., Ruthven, G., Bennett, V., Blackburn, J.P., Cox, C., Keung, C., Facey, T., Furber, M., Neufeld, C., Rockwell, R., Sarnik, A., Stein, J., "Active optical system design for the 4.2 m SOAR telescope", Proc. SPIE 4003, 122-135 (2000).
16. Bennet, R., Baine, F., "Active mirror support using pneumatic actuators", Proc. SPIE 5497, 91-102 (2004).
17. Smith, B., Chylek, T., Cuerden, B., DeGroff, B., Lotz, P.J., Venetiou, A., "The active optics system for the Discovery Channel Telescope", Proc. SPIE 7739, 77391T (2010).
18. Roddier, N., Blanco, D., Goble, L., Roddier, C., "The WIYN telescope active optics system", Proc. SPIE 2479, 364-376 (1995).
19. Martin, H.M., Callahan, S.P., Cuerden, B., Davison, W.B., DeRigne, S.T., Dettmann, L.R., Parodi, G., Trebisky, T.J., West, S.C., Williams, J.T., "Active supports and force optimization for the MMT primary mirror", Proc. SPIE 3352, 412-423 (1998).
20. Schechter, P.L., Burley, G., Hull, C., Johns, M., Martin, B., Schaller, S., Shectman, S.A., West, S.C., "Active optics on the Baade 6.5-m (Magellan I) telescope", Proc. SPIE 4837, 619-627 (2003).
21. Martin, H.M., Cuerden, B., Dettmann, L.R., Hill, J.M., "Active optics and force optimization for the first 8.4 m LBT mirror", Proc. SPIE 5489, 826-837 (2004).
22. Jared, R.C., Arthur, A.A., Andreae, S., Biocca, A., Cohen, R.W., Fuertes, J.M., Franck, J., Gabor, G., Liacer, J., Mast, T., Meng, J., Merrick, T., Minor, R., Nelson, J., Orayani, M., Salz, P., Schaefer, B., Witebsky, C., "The W.M. Keck telescope segmented primary mirror active control system", Proc. SPIE 1236, 996-1008 (1994).
23. Lefort, B., Castro, J., "The GTC primary mirror control system", Proc. SPIE 7019, 70190I (2008).
24. Neill, D., Angeli, G., Claver, C., Hileman, E., DeVries, J., Sebag, J., Xin, B., "Overview of the LSST active optics system", Proc. SPIE 9150, 91500G (2014).
25. Schipani, P., et al., "The VLT Survey Telescope: what stands behind the surveys", Astrophys. Space Sci. Proc. 42, in press (2016)
26. Kuijken, K., "OmegaCAM: ESO's newest imager", The Messenger 146, 8-11 (2011).
27. Capaccioli, M., Schipani, P., "The VLT Survey Telescope opens to the sky: history of a commissioning", The Messenger 146, 2-6 (2011).
28. Schipani, P., Noethe, L., Kuijken, K., Arcidiacono, C., Argomedo, J., Dall'Ora, M., D'Orsi, S., Farinato, J., Magrin, D., Marty, L., Ragazzoni, R., Umbriaco, G., "The VST alignment: strategy and results", Proc. SPIE 8444, 844456 (2012).
29. Noethe, L., Schipani, P., Holzlöhner, R., Rakich, A., "A method for the use of ellipticities and spot diameters for the measurement of aberrations in wide-field telescopes", Advanced Optical Technologies 3, 315-334 (2014).
30. Noethe, L., "Use of minimum energy modes for modal-active optics corrections of thin meniscus mirrors", J. Mod. Opt. 38 (6), 1043-1066 (1991).
31. Holzlöhner, R., Rakich, A., Noethe, L., Kuijken, K., Schipani, P., "Fast active optics control of wide-field telescopes based on science image analysis", Proc. SPIE 9151, 915112I (2014).
32. Shack, R., Thompson, K., "Influence of alignment errors of a telescope system on its aberration field", Proc. SPIE 251, 146-153 (1980).
33. Schmid, T., Rolland, J., Rakich, A., Thompson, K., "Separation of the effects of astigmatic figure error from misalignments using Nodal Aberration Therory (NAT)", Opt. Express 18, 17433-17447 (2010).
34. Schmid, T., Thompson, K., Rolland, J., "Misalignment induced nodal aberration fields in two-mirror astronomical telescopes", Appl. Opt. 49, D131-D144 (2010).
35. Schmid, T., Thompson, K., Rolland, J., "A unique astigmatic nodal property in misaligned Ritchey-Chrétien telescopes with misalignment coma removed", Opt. Express 18, 5282-5288 (2010).
36. Schechter, P., Levinson, R., "Generic misalignment aberration patterns in wide-field telescopes", PASP 123, 812-832 (2011).
37. Perrotta, F., Schipani, P., "A simulation model for a telescope earthquake analysis: the VST primary mirror safety system", Exp. Astron. 29, 189-206 (2011).
38. Schipani, P., D'Orsi, S., Fierro, D., Ferragina, L., Marty, L., Molfese, C., Perrotta, F., "Active optics primary mirror support system for the 2.6 m VST telescope", Appl. Opt. 49, 1234-1241 (2010).
39. Schipani, P., Perrotta, F., Marty, L., "Active Optics Correction Forces for the VST 2.6m primary mirror", Proc. SPIE 6273, 62733A (2006).
40. Schwesinger, G., "Lateral Support of very large telescope mirrors by edge forces only", J. Mod. Opt. 38 (8), 1507-1516 (1991).
41. Schipani, P., Marty, L., Perrotta, F., Magrin, D., D'Orsi, S., "The primary mirror system control software for the VST", Proc. SPIE 7740, 774037 (2010).
42. Schipani, P., Marty, L., "Stewart platform kinematics and secondary mirror aberration control", Proc. SPIE 6273, 62733B (2006).
43. Schipani, P., D'Orsi, S., Fierro, D., Marty, L., "Active optics control of the VST telescope secondary mirror", Appl. Opt. 49, 3199-3207 (2010).
44. Roddier, F., "Curvature sensing and compensation: a new concept in adaptive optics", Appl. Opt. 27, 1223-1225 (1988).
45. Roddier, C., Roddier, F., "Wavefront reconstruction from defocused images and the testing of ground-based optical telescopes", J. Opt. Soc. Am. A 10, 2277-2287 (1993).
46. Kuijken, K., Baruffolo, A., Bagnara, P., Magagna, C., "The OmegaCAM Real-Time Image Analysis System", Proc. SPIE 5492, 494-499 (2004).
47. Schipani, P., Noethe, L., Arcidiacono, C., Argomedo, J., Dall'Ora, M., D'Orsi, S., Farinato, J., Magrin, D., Marty, L., Ragazzoni, R., Umbriaco, G., "Removing static aberrations from the active optics system of a wide-field telescope", J. Opt. Soc. Am. A 29, 1359-1366 (2012).